# Water-hydroxide trapping in cobalt tungstate for proton exchange membrane water electrolysis

Ranit Ram[1†], Lu Xia[1†], Hind Benzidi[2†], Anku Guha[1†], Viktoria Golovanova[1], Alba Garzón Manjón[3], David Llorens Rauret[3], Pol Sanz Berman[2], Marinos Dimitropoulos[1], Bernat Mundet[3], Ernest Pastor[4,5], Verónica Celorrio[6], Camilo A. Mesa[7], Aparna M. Das[1], Adrián Pinilla-Sánchez[1], Sixto Giménez[7], Jordi Arbiol[3,8], Núria López[2], F. Pelayo García de Arquer[1*]

[1]*ICFO – Institut de Ciències Fotòniques, The Barcelona Institute of Science and Technology, Castelldefels (Barcelona) 08860, Spain.*
[2]*ICIQ-CERCA – Institute of Chemical Research of Catalonia, The Barcelona Institute of Science and Technology, Tarragona 43007, Spain.*
[3]*Catalan Institute of Nanoscience and Nanotechnology (ICN2), CSIC and BIST, Campus UAB, Bellaterra, 08193 Barcelona, Catalonia, Spain.*
[4]*CNRS, Univ Rennes, IPR (Institut de Physique de Rennes) - UMR 6251, Rennes, France.*
[5]*CNRS, Univ Rennes, DYNACOM (Dynamical Control of Materials Laboratory) - IRL2015, The University of Tokyo, 7-3-1 Hongo, Tokyo 113-0033, Japan.*
[6]*Diamond Light Source, Harwell Science and Innovation Campus, Didcot OX11 0DE, United Kingdom.*
[7]*Institute of Advanced Materials (INAM) Universitat Jaume I, 12006, Castelló, Spain.*
[8]*ICREA, Pg. Lluís Companys 23, 08010 Barcelona, Spain.*

[†]These authors contributed equally to this work

[*]correspondence to: pelayo.garciadearquer@icfo.eu

**The oxygen evolution reaction (OER) is the bottleneck to energy-efficient water-based electrolysis for production of $H_2$ and other solar fuels. In proton exchange membrane water electrolysis (PEMWE), precious metals have generally been necessary for stable catalysis of this reaction. Here, we report that delamination of cobalt tungstate enables high activity and durability via the stabilization of oxide and water-hydroxide networks of the lattice defects in acid. The resulting catalysts achieve lower overpotentials, a current density of 1.8 A·cm$^{-2}$ at 2 V, and stable operation up to 1 A·cm$^{-2}$ in a PEMWE system at industrial conditions (80ºC) at 1.77 V; a three-fold improvement in activity; stable operation at 1 A·cm$^{-2}$ over the course of 600 h.**

The increasing global energy demand, combined with the urgent need to abate climate change, has accelerated the development of sustainable and clean energy technologies alternative to fossil fuels. Water electrolysis (WE) to synthesize hydrogen ($H_2$), has emerged as a promising strategy to produce clean energy vectors from water and low carbon electricity, offering a path to decarbonize global industries such as energy, transport, manufacturing, and agriculture, among others (*1–3*).

Amongst the different water electrolysis technologies, the proton exchange membrane (PEMWE), in which cathode and anode electrodes are intimately connected through a proton conductive membrane, exhibits advantages compared to diaphragm and anion transport-based alternatives in terms of productivity (high current density operation), energy efficiency, stability, and levelized cost of hydrogen (*4–6*).

In this context, the efficient and sustainable large-scale production of $H_2$ through water electrolysis still faces important challenges. These are associated to the sluggish kinetics of the oxygen evolution reaction (OER) and the reliance on scarce, critical raw materials, such as iridium (Ir) – so far, the prevalent anode catalyst material based on its stability, but one of the least abundant metals on Earth (*7–9*).

Alternative approaches based on ruthenium (Ru) have shown promising activity, but suffer from a strong metal dissolution in acid media intrinsic to lattice oxygen evolution reaction mechanisms (*10–12*). There is, thus, an urgent need to develop efficient and stable Ir- and Ru-free anodes for PEMWE (*13–17*).

Transition metal oxides are interesting catalyst candidates for the OER, as their multiple oxidation states could promote activity in a wide pH range (*18, 19*). First row transition metal oxides have shown promising activity in the acidic OER (*20–25*). Among them, Co-, Ni- and Mn-based anodes, have received special attention considering their relative abundance and

activity prospects (*26, 27*). Based on theoretical calculations, the OER activity of Co-based oxides should be comparable with that of Ru- and Ir-oxides (*28*).

However, such prospective activity is challenged by the limited stability of $CoO_x$ in acid due to higher Co-ion dissolution (**Fig. 1A**), even at open circuit potential (*29, 30*). Several strategies have been proposed to stabilize cobalt oxides in highly concentrated proton environments. Fundamental progress in this direction has mostly been pursued in low-current H-cells controlling the valence and ratio of active species (*e.g.*, $Co^{2+}/Co^{3+}$) through doping with higher valence metals (Cr, Mn) (*22, 24, 25, 31*); controlling catalyst reconstruction (*32*); doping with hydrophobic carbon (*33*); and addressing the substrate-catalyst interaction (*29*).

Unfortunately, translating these findings into active and stable PEMWE based on more abundant alternatives to Ir and Ru remains an open challenge (*34*). In Mn systems, phase control ($\gamma$-$MnO_2$) led to stability improvements (12 h at 100 $mA \cdot cm^{-2}$), which gradually decreases as the $\gamma$-$MnO_2$ phase becomes permanganate ($MnO_4^-$) (*26*). Mn-oxybromide species resulted 300 h stability at 100 $mA \cdot cm^{-2}$ (0.41 $mV \cdot h^{-1}$ degradation) (*23*). In Co-based electrodes, La and Mn doping has enabled a ~0.6 $A \cdot cm^{-2}$ current density at 2 V, and 110 h stability at 210 $mA \cdot cm^{-2}$ (~1.65 V at 80°C) (*25*). These experimental observations showcase the challenges in achieving Ir/Ru-free PEMWE anodes that break the activity-stability trade-off through conventional doping schemes.

Recent works have highlighted the potential of controlling the other half of the electrochemical interface (*i.e.*, water structure and adsorbed oxide species), to improve the OER. The participation of oxygen from adsorbed water in the OER, as opposed to lattice-mediated, would decrease metal dissolution and increase stability (*25*). In general, the interaction of adsorbed bridging oxygen ($O_{bri}$) species with water could open new reaction pathways (*35*). Theoretical studies have shown the critical role of H–bonding network of interfacial water and their impact on proton-electron transfer steps (*36, 37*). Decreasing the degree of H–bonding of interfacial

water (*n*–HB·$H_2O$), has been predicted to reduce the activation energy needed to dissociate water (*38*). The role of interfacial water and hydrogen bonding network, already studied for the hydrogen evolution reaction (*39*), is largely overlooked for acidic OER.

This prompted us to jointly address the water and oxide structure, a so far underexplored path, seeking to improve activity and stability in non-Ir PEMWE anodes.

Here, we demonstrate control over the OER reaction by modulating the interfacial water structure and intermediate species in a delaminated CoW-oxide lattice (**Fig. 1B-D**), resulting in active and stable PEMWE. We achieve this by implementing a delamination strategy whereby high-valence sacrificial elements such as W, when incorporated in a $CoWO_4$ (CWO) crystal structure, could be selectively eliminated in a subsequent water/hydroxide-$WO_4^{2-}$ anion exchange process (**Fig. 1C**). This results in structural delamination and in the subsequent trapping and stabilization of water and hydroxide species in a Co-oxide defect network. Such water-hydroxide shielding renders the Co ion dissolution thermodynamically unfavorable for the delaminated CWO in contrast to $Co_3O_4$ (**Fig. 1D** and Table S1) showing a drastic decrease in Co ion dissolution in acid (Fig. S1).

The delaminated (CWO–del) catalysts achieve remarkable performance in a PEMWE, with a 1.8 A·$cm^{-2}$ current density at 2 V – up to a three-fold improvement compared the previous best performance for non-Ir/Ru (*25, 40*) – and stable operation of 608 h at the current density of 1 A·$cm^{-2}$ (**Fig. 1E, F**).

**Anion-exchange delamination controls water structure in acid**

To incorporate and stabilize $OH^-/H_2O$ into the lattice of $MM'_xO_y$ (M: Mn, Co, Ni, Cu), we devised an anion exchange strategy whereby lattice oxyanions (*e.g.*, $M'_xO_y^{z-}$, M': S, Mo, W), would be delaminated and exchanged by $OH^-/H_2O$ species as follows:

$$MM'_xO_y + m\,H_2O + n\,OH^- \rightarrow M\left(M'_xO_y\right)_{1-q}(H_2O)_m(OH)_n + q\,M'_xO_y^{z-} \qquad (1)$$

The design principles require that such oxyanions have adequate binding energies with $OH^-$ and water species, conditions that promote their sacrificial leaching (*41*), and that the host lattice could accommodate $OH^-/H_2O$ species to saturate the resulting oxyanion vacancies (suppl. Section 4, Table S4-S6). Our initial theoretical calculations predicted that $WO_4^{2-}$ ions, compared to other anions such as molybdate or sulfate, provide more favorable defect energy to meet these criteria: The energy associated with defect formation upon removing $WO_4^{2-}$ from the $CoWO_4$ is the lowest energy among $SO_4^{2-}$ and $MoO_4^{2-}$ removal from $CoSO_4$ and $CoMoO_4$, respectively (suppl. Section 4, Fig. S2).

We thus synthesized CWO using a hydrothermal reaction (suppl. Section 1, Fig. S3). The sharp peaks in X-ray diffraction (XRD) patterns from different batches indicate a highly crystalline structure matching a monoclinic $CoWO_4$ phase, and the high reproducibility of the synthesis procedure (Fig. S4, S5).

To perform the $WO_4^{2-} \rightarrow OH^-/H_2O$ anion exchange, we explored a base treatment dispersing the resulting CWO material in an 0.1 M KOH aqueous solution for different time periods (suppl. Section 3, Fig. S6, S7). We studied the effects of cation ($Li^+$ to $Cs^+$), solvent ($H_2O$, DMSO, NMP), and pH (both experimental and theoretical) in the process (suppl. Section 3, Fig. S8-S13). This study revealed the critical role of $K^+$ to balance the delamination and the need for $H_2O$ to enable the anion exchange. CWO–del samples retained structural stability after 72 h immersion in 0.5 M $H_2SO_4$, as opposed to Co controls (Fig. S14).

Powder XRD patterns show a regular shift in the most intense $\bar{1}11$ peak (Table S7), indicating the generation of defects/strain in the crystal structure while the bulk monoclinic crystal phase remains intact. These are consistent with optoelectronic, magnetic and x-ray absorption spectroscopy studies, showing the increased formation of vacancies and defects (Fig. S15-S19). Transmission electron micrographs (TEM) and scanning transmission electron micrographs (STEM) show a shape transition from a cube-like CWO (Fig. S20, S21), to a delaminated, flake-like shape, after KOH treatment (Fig. S22, S23). The size of the particles after delamination remains comparable to CWO (Fig. S24).

High resolution-TEM (HRTEM) images reveal the missing regular (010) crystal plane in CWO–del–48 (Fig. S22, S25), indicative of defects arising from $WO_4^{2-}$ leaching. High annular angle dark field STEM images (HAADF-STEM), and respective energy-dispersive X-ray spectroscopy (EDS) mapping of Co and W, show the uniform distribution of Co and W throughout the pristine and delaminated nanocrystals (Fig. S26, S27). The electron energy loss spectra (EELS) indicate a reduction in the Co/W atomic ratio after delamination (Fig. S28). Additionally, atomic force microscopy (AFM) reveals missing planes and corresponding defects in CWO–del–48 (Fig. S29-31), in agreement with HRTEM and STEM results.

To assess the atomic arrangement of Co and W sites, we performed integrated differential phase contrast (iDPC) STEM images (Fig. S32). CWO samples exhibit a regular atomic arrangement of Co, W and O atoms consistent to a monoclinic phase. CWO–del–48, on the other hand, reveals a substantial amount of vacancies due to $WO_4^{2-}$ leaching (Fig. S33).

To get more insights on the dynamics of the oxyanion exchange, we performed *ex situ* Raman measurements at different delamination times. These reveal a bathochromic shift (~5–10 $cm^{-1}$) for both Co–O (~690 $cm^{-1}$) and W–O (~886 $cm^{-1}$) peaks with increasing delamination time (**Fig. 2A**). The intensity ratio of Co–O to W–O peaks increases up to 48 h, and then saturates (**Fig. 2A**, inset; Fig. S34 and Table S8). This suggests a kinetic limitation of W-leaching from

the CWO-matrix. Inductively-coupled plasma optical emission spectroscopy (ICP-OES) measurements confirm increasing W leaching over time, but negligible change in Co concentration (Fig. S35 and Table S9). The optimal Co/W ratio and $OH^-/H_2O$ trapping considering initial electrochemical studies is achieved for 48 h-delaminated samples (details in later sections). DFT simulations show that (010) is the most thermodynamically favorable crystal facet for delamination process which is exothermic only at high pH (Fig. S36-S38 and Table S10, S11, Movie S1).

**Water trapping and hydroxide bridging**

To assess the presence of water and $OH^-$ ions in the delaminated samples, we carried out a series of characterizations. Thermogravimetric analysis coupled with mass spectroscopy (TGA-MS) revealed a ~16% weight loss for CWO−del−48 over a 166°C to 396°C range due to water and/ or $OH^-$ ions, which is negligible for CWO and $Co_3O_4$ (**Fig. 2B** and S39). Four distinct peaks in this range suggest the presence of different water coordination environments (*42*).

To assess these differently coordinated water populations, we initially performed Fourier-transform infrared (FTIR) measurements. These reveal HO–H stretching and H–O–H bending vibrational modes with increasing intensity upon delamination, suggesting a higher density of trapped and bridged water and hydroxide groups within the crystals (Fig. S40). Further, the narrow single H−OH stretching peak present in the *ex situ* Raman spectrum of CWO−del−48, indicates the presence of highly H-bonded water (**Fig. 2B** inset and Fig. S41) (*43*).

Additionally, we replaced $H_2O$ with $D_2O$ during the delamination process and subjected the samples to mild annealing. This resulted in distinct spectral features corresponding to a D−OD stretching mode, confirming the trapping of $D_2O/H_2O$ in the delaminated materials (Fig. S42) (*44*).

We studied the resulting oxygen modes using x-ray photo electron spectroscopy (XPS) (**Fig. 2C**). The O 1s peak of non-delaminated samples deconvolutes into two peaks at 528.55 eV and 530.33 eV, which correspond to metal oxygen ($O_M$) and lattice oxygen ($O_L$) (*25*). CWO–del–48 spectra, on the other hand, require deconvolution into two additional peaks corresponding to hydroxide ($O_{OH}$, at 531.6 eV) and water species ($O_{H_2O}$, at 533.1 eV) (*35*). The $O_M$ and $O_L$ peaks blue shift in this case, which is consistent with the leaching of W in the form of $WO_4^{2-}$ and associated atomic-vacancies ($O_M$) (*45*); also supported by UV-Vis, EPR and XANES spectra (Fig. S15-S19). The amplitude of $O_{OH}$ and $O_{H_2O}$ signals further suggests the presence of hydroxide and bonded water in the delaminated compound.

To gain insights on the role of delamination and water-hydroxide trapping in rendering catalyst stability, we carried out DFT studies considering water trapping and hydroxide bridging from $WO_4^{2-}$ sites transformation (Movie S1, Fig. S12). As the size of water trapped structures can also vary, various combinations of structures with different numbers of water molecules and $OH^-$ were calculated. Among the different combinations of CWO-water-hydroxide, $Co(WO_4)_{1-x}(H_2O)_2(OH)_2$ is the thermodynamically most favorable delaminated species, with a –4.5 eV of Gibbs free energy change for the transformation (**Fig. 2D,** Table S12, S14**)**. The calculated Pourbaix diagram (**Fig. 2E**) confirm the stability of this phase over other structures at pH 0.

The blue shift observed in XANES and distinct EXAFS spectra imply a higher oxidation state of Co and a modified coordination environment in CWO–del–48 compared to CWO (Fig. S18, S19). The corresponding Co–O and Co–Co bond distance of CWO–del–48 structure is shorter than that in CWO (Fourier-transformed EXAFS, Fig. S19 and crystal structure, Fig. S43), which could facilitate higher valence Co-species, such as CoOOH, Co-peroxide, in OER (*20, 31, 46*).

*In situ* Raman spectroscopy in 0.5 M $H_2SO_4$ electrolyte reveals three oxide peaks at 1.7 V (*vs.* RHE) (suppl. Section 6, Table S2, S3), some of which are not visible in *ex situ* Raman (**Fig.**

**2F**). These correspond to layered β–CoOOH (~502 $cm^{-1}$), γ–CoOOH (~571 $cm^{-1}$), and higher oxidation $Co^{IV}$–O (~840 $cm^{-1}$), and Co–peroxide (~1080 $cm^{-1}$) sites (*46–48*), in agreement with EXAFS, XPS and DFT findings (Fig. 2C, S19, and S44).

**Structural influence on the OER mechanism**

To gain more insights into the peroxide species and the nature of the active sites ensuing from $OH^-/H_2O$ trapping, we performed additional operando Raman spectroscopy studies before and after OER onset potential (**Fig. 3A**, Fig. S43). Both β–CoOOH and Co-peroxide peak intensities steadily increase from open circuit potential (OCP) to 1.9 V *vs.* RHE, and vanish as the potential is cycled back to OCP from 1.9 V *vs.* RHE (**Fig. 3A**). This suggests that both β–CoOOH and Co-peroxide are active sites for the OER.

To investigate the role of the surface-oxides and water-hydroxide trapping in the OER activity, we carried out a suite of pH-dependent electrochemical studies and *operando* interfacial water structure evaluation using Raman.

Delaminated samples display a very strong pH-dependence during the OER, with a reaction order ($\rho$) of –0.84, nearly 2.5 times than that for CWO (**Fig. 3B**). This can be explained by the presence of trapped water and a higher $OH^-$ coverage, in agreement with both XPS (**Fig. 2D**) and FTIR studies (Fig. S40). The calculated cross-sectional crystal structure (Fig. S43) and XPS analysis (Fig. S45), suggest a CoOOH-rich arrangement where water is bonded with Co atoms through the oxygen. This is consistent with Raman findings and methanol oxidation reaction (MOR) experiments, showing a dominance of MOR over water dissociation in CWO–del–48 across different pH values, in line with the higher amount of surface oxides (**Fig. 3C**) (*49*).

Next, we studied the role of interfacial H–OH using *operando* Raman (Fig. S46, S47), deconvoluting three different water structures depending on the number of H–bonds: 4-H–bonded water (~3200 $cm^{-1}$), 3-H–bonded water (~3400 $cm^{-1}$) and 0-H–bonded water

(~3600 $cm^{-1}$). The activation energy required for water dissociation is predicted to decrease with decreasing degree of H-bonding (*39*). As the potential increases from 0.4 V to 1.9 V *vs.* RHE, the relative presence of 4–HB·$H_2O$ in CWO–del–48 decreases from 35% to 5%, whereas 0–HB·$H_2O$ increases from 4% to 68% (**Fig. 3D**). In contrast, these remain unchanged for CWO throughout the applied potential window. This observation suggests the involvement of interfacial water in the RDS for CWO–del–48 catalyst. Moreover, the significant change in the Stark slope explains the higher sensitivity of interfacial water structure after OER onset potential (Fig. S48).

Based on these experimental observations, we performed DFT calculations to assess the energy landscape of the OER mechanisms using the computational hydrogen electrode (CHE) formalism (**Fig. 3E**). We denote the paths where the confined water fragments can also participate as confined paths. The oxide path mechanism (OPM) has a common RDS (*OH–O* to *O–O*) for both CWO and for the confined water fragments in CWO–del–48 without involving interfacial water. The RDS for CWO–del–48 is 0.09 eV smaller for the OPM pathway than for the adsorbate evolution mechanism (AEM), making it thermodynamically more plausible. In the AEM pathway (suppl. Section 4), the RDS is however different: $OH^*$-to-$O^*$ for CWO *vs*. the confined system cAEM, O*-to-OOH* for CWO–del–48 (Suppl. Table S14-S17). The higher pH dependence and change of the interfacial water structure with increasing applied potential for CWO–del–48, suggests that CWO–del–48 benefits from the kinetically favorable AEM mechanism (**Fig. 3F,** S17).

To gain insights into the improved acid resistance under electrolytic conditions, we revisited the surface Pourbaix diagram of CWO–del (**Fig. 2E**). This diagram is divided into five distinct regions: I: $CWO(H_2O)_2(OH)_2$, II: $CWO(H_2O)_3OOH^*$, III: $CWO(H_2O)_3OH^*O^*$, IV: $CWO(H_2O)_3{}^*OO^*$, and V: $CWO(H_2O)_3O^*$ (details in suppl. Fig. S49). In conditions of low pH, the $H^+$ ions from the acidic environment interact with $H_2O$–OH cluster in

$CWO(H_2O)_2(OH)_2$ (region I), which transforms into $CWO(H_2O)_3OH^*O^*$ (region III). When the potential lies between 1.2 V and 1.37 V *vs.* RHE, interfacial water molecules (region I) interact with another surface oxygen to form a hydroxyl group: $O^* + H_2O \rightarrow OOH^* + H^+ + e^-$, the cation on the surface undergoes oxidation and is stabilized by OOH*. Simultaneously, the oxygen on the surface binds with H* to create a stable structure of $CWO(H_2O)_3{}^*OO^*$ (region IV), and the two O* species combine directly to form $O_2$, leading to the release of oxygen without the formation of *OOH intermediate. As the potential rises to ≥ 1.46 V (*vs*. RHE), the surface is shielded by O* leading to the formation of a stable $CWO(H_2O)_3O^*$ structure (region V).

**Electrochemical performance**

We compared the polarization curves of CWO–del catalysts with commercial $Co_3O_4$ and $IrO_2$ (**Fig. 4A**) (suppl. Section 6). A minimum 288 mV overpotential at 10 $mA{\cdot}cm^{-2}$ current density was obtained for CWO–del–48 (no *iR* correction), as opposed to 392 mV and 259 mV for commercial $Co_3O_4$ and $IrO_2$ respectively (see Fig. S50-52 and Table S18 for details on particle size, loading, and double layer capacitance). Statistical analysis (**Fig. 4B**) and extended measurements confirm the reproducibility of these trends (Fig. S53-S54). The Faradaic efficiency for $O_2$ generation was 96.6 ± 5.2% at 10 $mA{\cdot}cm^{-2}$ current density (Fig. S55-S60).

Tafel analysis reveals a slope 85 $mV{\cdot}dec^{-1}$ for CWO–del–48, *vs.* 63 $mV{\cdot}dec^{-1}$ for $IrO_2$ and 227 $mV{\cdot}dec^{-1}$ for CWO. This showcases the improved OER kinetics of CWO–del–48 over reference samples, approaching that of $IrO_2$ (Fig. S61).

CWO–del–48 exhibits the highest stability (>175 h) over commercial $Co_3O_4$ and CWO (**Fig. 4C**) in H-cell at 10 $mA{\cdot}cm^{-2}$. Structural, compositional, and electrochemical post-analysis, suggest that the crystallinity, microstructure and size, remain comparable after electrolysis (Fig. S24, S62-67, Table S19).

We then assessed Co leaching and the potential role of dissolved species. Inductively coupled plasma-mass spectroscopy (ICP-MS) reveals that Co leaching remains unchanged after 50 h of OER in H-cell at 10 mA·cm$^{-2}$, with a ~2.76 ppm concentration of dissolved Co ions in anolyte after 100 h of chronopotentiometry (Fig. S68). A fraction of Co ions (0.3 ppm) leaches out during OCP, pre-OER stability test. The concentration of dissolved Co ions in the catholyte remained negligible (< 30 ppb, Fig. S69), and no traces were found in the membrane (Fig. S70, Table S20) or graphite rod (Fig. S71). The resulting stability number (S-number) (*50, 51*) after 100 h of stability test at 10 mA·cm$^{-2}$ is 14771 $\pm$ 768 (Fig. S72). Additional experiments confirm the electrochemical stability at different mass loadings (0.075 to 2 mg·cm$^{-2}$) (Fig. S73, S74).

Encouraged by this, we implemented the CWO–del–48 catalyst in a PEMWE system (**Fig. 4D,** S75) and studied the cell performance under industrial operational settings, including 80°C temperature and high current density of 0.2 – 1 A·cm$^{-2}$ (see methods and suppl. section 6 for details). The polarization curve of CWO–del–48 based cells reaches a nominal current density of 1.8 A·cm$^{-2}$ at 2 V (**Fig. 4E**); an improvement in rate over the previous-best non-Ir/Ru anodes of up to 3× for a comparable membrane (*25*) and of 1.8× for advanced, thinner membranes (*40*). During electrolysis at a fixed current density of 0.2 A·cm$^{-2}$, the voltage range (1.53 – 1.56 V) is ~130 mV lower than prior-best Co-based PEMWE catalysis (**Fig. 4F**) and matches that of Ir black (1.50 V) at ¼ the loading. This showcases the potential of CWO–del–48 catalysts compared to the well-established iridium oxide, along with its lower cost, and potentially higher availability of Co and W. This performance (~1.52 V at 0.2 A·cm$^{-2}$) is retained for at least over 278 h continuous operation (limited by pump failure).

ICP-OES analysis of the anolyte reveals a Co concentration of ~1.7 ppm after 20 h of electrolysis (Fig. S76). We additionally performed single pass electrolyte flow experiments to study the potential role of ion accumulation in the electrolyte reservoir. The cell voltage

remains stable (within 1.53-1.54 V) for at least 32 h at 0.2 $A \cdot cm^{-2}$ at similar PEMWE conditions but continuous, fresh electrolyte flushing (Fig. S77).

We further challenged the stability of the CWO–del–48 catalyst at 1 $A \cdot cm^{-2}$ operation (**Fig. 4F**) – a so far elusive benchmark for Ir/Ru-free catalysts. Electrodes show comparable composition after an initial 20 h study (Fig. S78-S81, Table S21). The PEMWE cell exhibited stable performance, with a stabilized cell voltage of ~1.77 V during a 608 h of durability study (see table S22 for prior benchmarks). The observed slight voltage fluctuations might arise due to a combination of temperature gradients during electrolyte replenishment, modifying electrolysis rates and gas dissolution, as well as catalyst dissolution (ion and particulate detachment) events.

The calculated S-number at these conditions is ~31% of that achieved at 10 $mA \cdot cm^{-2}$ in the H-cell (supplementary text). This showcases the impact of high rate and temperature operation stress, which accelerate catalyst degradation.

**Conclusion and future scope**

The reported strategy still faces several challenges and opportunities. CWO–del samples exhibit high polarization voltage under high current density, which should be improved by further optimization of the integration of key components, to enhance electrolysis performance and subsequently improve stability at higher currents that approach state-of-the-art Ir-systems. In the future, achieving industrial performance benchmarks, such as energy-efficient and stable operation in the 2-3 $A \cdot cm^{-2}$ range (a milestone of $IrO_2$ in PEMWE), will require tailored engineering of catalysts electrodes and membranes. In that sense, obtaining further insights on the properties of these interfaces, and on the role of water trapping and hydroxide bridging, in the OER at increasing current densities, will be crucial. Operando spectroscopies and modelling at these settings are fundamental enabling tools that can help in that direction. Quantifying the catalyst dissolution dynamics through inline ICP-MS studies, under relevant

PEMWE target conditions, is crucial to further understand the local dissolution-redeposition equilibria. Combined with morphology and elemental analysis, this could help elucidate the dissolution pathways through accelerated stress tests (*52*).

Progressing towards fully earth-abundant metal PEMWE catalysts, including the cathodic side, and recyclable systems, demands further innovation spanning materials, electrode structures, membranes-electrode interface, and process control. While this study focuses on abundant Co-based OER catalysts, further advances in alternative materials (*e.g.*, Mn, Ni), which consider geopolitical barriers and environmental aspects related to metal extraction and purification, remain urgently needed.

**Acknowledgements**

**Funding:** ICFO thanks the Fundació Cellex, Fundació Mir-Puig, and the La Caixa Foundation (100010434, E.U. Horizon 2020 Marie Skłodowska-Curie grant agreement 847648), and 2022 Leonardo Grant for Researchers in Physics, BBVA Foundation. ICIQ thanks the Spanish Ministry of Science and Innovation (Ref. No. PID2021-122516OB-I00, and the Barcelona Supercomputing Center (BSC-RES) for providing computational resources. ICN2 acknowledges funding from Generalitat de Catalunya through 2021SGR00457, IU16-014206 (METCAM-FIB); the Advanced Materials programme supported by the MCIN with European Union NextGenerationEU (PRTR-C17.I1) and Generalitat de Catalunya funds; NANOGEN (PID2020-116093RB-C43) and RED2022-134508-T (CAT&SCALE), funded by MCIN/ AEI/10.13039/501100011033/ and by "ERDF A way of making Europe", by the "European Union"; AGM thanks Grant RYC2021 - 033479. Authors acknowledge the use of instrumentation and advice provided by the Joint Electron Microscopy Center at ALBA (JEMCA), and the Diamond Light Source for access to the I18 beamline. ICFO (CEX2019-000910-S), ICIQ (CEX2019-000925-S), and ICN2 (CEX2021-001214-S) thank Severo Ochoa Center of Excellence (MCIN/AEI/10.13039/501100011033) funding and CERCA, and Generalitat de Catalunya. S.G. thanks PID2020-116093RB-C41 funded by MCIN/ AEI/10.13039/501100011033. CAM thanks the Generalitat Valenciana (APOSTD/2021/251) and the MinCiencias Colombia through the Fondo Nacional de Financiamiento para la Ciencia, la Tecnología y la Innovación "Francisco José de Caldas", call 848-2019. EP acknowledges the support from the CNRS and the French Agence Nationale de la Recherche (ANR), under grant ANR-22-CPJ2-0053-01. Funded/Co-funded by the European Union (ERC, PhotoDefect, 101076203). Views and opinions expressed are however those of the authors only and do not necessarily reflect those of the European Union or the European Research Council. Neither the European Union nor the granting authority can be held responsible for them.

**Author Contributions**

FPGA proposed and supervised the project. RR designed, conducted the experiments, data analysis of electrochemical experiments, crystallography, microscopy and spectroscopic experiments. LX led the PEMWE implementation, data analysis and illustrations. HB, PSB, and NL carried out DFT calculations. AG and APS optimized *in situ* Raman spectroscopy setup. AG performed *in situ* Raman spectroscopy experiments and electrochemical data analysis. VG performed SEM. AGM, BM, DLR and JA conducted and analysed STEM experiments. VC, CAM, EP and SG carried out XAS experiments and data analysis. MD

carried out AFM experiments and data analysis. AMD performed XRD. RR, LX, AG and FPGA composed manuscript. All authors discussed the results, edited, and commented on the manuscript.

**Competing interests:** R.R., L.X., A.G, F.P.G.A are inventors on patent application EP147926 submitted by ICFO that covers the OER catalyst reported herein.

**Data and materials availability:**

A data set collection of computational results is available in an ioChem-BD repository (*53*). STEM and X-ray diffraction data files are available in Zenodo (*54*).

**References:**


1. S. Chu, A. Majumdar, Opportunities and challenges for a sustainable energy future. *Nature* **488**, 294–303 (2012).
2. I. Staffell, D. Scamman, A. Velazquez Abad, P. Balcombe, P. E. Dodds, P. Ekins, N. Shah, K. R. Ward, The role of hydrogen and fuel cells in the global energy system. *Energy Environ Sci* **12**, 463–491 (2019).
3. Z. W. Seh, J. Kibsgaard, C. F. Dickens, I. Chorkendorff, J. K. Nørskov, T. F. Jaramillo, Combining theory and experiment in electrocatalysis: Insights into materials design. *Science* **355**, eaad4998 (2017).
4. M. Carmo, D. L. Fritz, J. Mergel, D. Stolten, A comprehensive review on PEM water electrolysis. *Int J Hydrogen Energy* **38**, 4901–4934 (2013).
5. C. Spöri, J. T. H. Kwan, A. Bonakdarpour, D. P. Wilkinson, P. Strasser, The Stability Challenges of Oxygen Evolving Catalysts: Towards a Common Fundamental Understanding and Mitigation of Catalyst Degradation. *Angewandte Chemie International Edition* **56**, 5994–6021 (2017).
6. L. An, C. Wei, M. Lu, H. Liu, Y. Chen, G. G. Scherer, A. C. Fisher, P. Xi, Z. J. Xu, C.-H. Yan, Recent Development of Oxygen Evolution Electrocatalysts in Acidic Environment. *Advanced Materials* **33**, 2006328 (2021).
7. P. C. K. Vesborg, T. F. Jaramillo, Addressing the terawatt challenge: scalability in the supply of chemical elements for renewable energy. *RSC Adv* **2**, 7933–7947 (2012).
8. L. Yang, G. Yu, X. Ai, W. Yan, H. Duan, W. Chen, X. Li, T. Wang, C. Zhang, X. Huang, J.-S. Chen, X. Zou, Efficient oxygen evolution electrocatalysis in acid by a perovskite with face-sharing $IrO_6$ octahedral dimers. *Nat Commun* **9**, 5236 (2018).
9. Y. Pi, Q. Shao, P. Wang, J. Guo, X. Huang, General Formation of Monodisperse IrM (M = Ni, Co, Fe) Bimetallic Nanoclusters as Bifunctional Electrocatalysts for Acidic Overall Water Splitting. *Adv Funct Mater* **27**, 1700886 (2017).
10. S. Cherevko, A. R. Zeradjanin, A. A. Topalov, N. Kulyk, I. Katsounaros, K. J. J. Mayrhofer, Dissolution of Noble Metals during Oxygen Evolution in Acidic Media. *ChemCatChem* **6**, 2219–2223 (2014).

11. E. A. Paoli, F. Masini, R. Frydendal, D. Deiana, C. Schlaup, M. Malizia, T. W. Hansen, S. Horch, I. E. L. Stephens, I. Chorkendorff, Oxygen evolution on well-characterized mass-selected Ru and $RuO_2$ nanoparticles. *Chem Sci* **6**, 190–196 (2015).

12. A. Grimaud, O. Diaz-Morales, B. Han, W. T. Hong, Y.-L. Lee, L. Giordano, K. A. Stoerzinger, M. T. M. Koper, Y. Shao-Horn, Activating lattice oxygen redox reactions in metal oxides to catalyse oxygen evolution. *Nat Chem* **9**, 457–465 (2017).

13. Z.-Y. Wu, F.-Y. Chen, B. Li, S.-W. Yu, Y. Z. Finfrock, D. M. Meira, Q.-Q. Yan, P. Zhu, M.-X. Chen, T.-W. Song, Z. Yin, H.-W. Liang, S. Zhang, G. Wang, H. Wang, Non-iridium-based electrocatalyst for durable acidic oxygen evolution reaction in proton exchange membrane water electrolysis. *Nat Mater* **22**, 100–108 (2023).

14. L. C. Seitz, C. F. Dickens, K. Nishio, Y. Hikita, J. Montoya, A. Doyle, C. Kirk, A. Vojvodic, H. Y. Hwang, J. K. Norskov, T. F. Jaramillo, A highly active and stable IrOx/$SrIrO_3$ catalyst for the oxygen evolution reaction. *Science* **353**, 1011–1014 (2016).

15. S. Hao, H. Sheng, M. Liu, J. Huang, G. Zheng, F. Zhang, X. Liu, Z. Su, J. Hu, Y. Qian, L. Zhou, Y. He, B. Song, L. Lei, X. Zhang, S. Jin, Torsion strained iridium oxide for efficient acidic water oxidation in proton exchange membrane electrolyzers. *Nat Nanotechnol* **16**, 1371–1377 (2021).

16. Y. Wang, S. Hao, X. Liu, Q. Wang, Z. Su, L. Lei, X. Zhang, Ce-Doped $IrO_2$ Electrocatalysts with Enhanced Performance for Water Oxidation in Acidic Media. *ACS Appl Mater Interfaces* **12**, 37006–37012 (2020).

17. H. Liu, Z. Zhang, J. Fang, M. Li, M. G. Sendeku, X. Wang, H. Wu, Y. Li, J. Ge, Z. Zhuang, D. Zhou, Y. Kuang, X. Sun, Eliminating over-oxidation of ruthenium oxides by niobium for highly stable electrocatalytic oxygen evolution in acidic media. *Joule* **7**, 558–573 (2023).

18. M. W. Kanan, D. G. Nocera, In Situ Formation of an Oxygen-Evolving Catalyst in Neutral Water Containing Phosphate and $Co^{2+}$. *Science* **321**, 1072–1075 (2008).

19. J. B. Gerken, J. G. McAlpin, J. Y. C. Chen, M. L. Rigsby, W. H. Casey, R. D. Britt, S. S. Stahl, Electrochemical Water Oxidation with Cobalt-Based Electrocatalysts from pH 0–14: The Thermodynamic Basis for Catalyst Structure, Stability, and Activity. *J Am Chem Soc* **133**, 14431–14442 (2011).

20. Z.-F. Huang, J. Song, Y. Du, S. Xi, S. Dou, J. M. V. Nsanzimana, C. Wang, Z. J. Xu, X. Wang, Chemical and structural origin of lattice oxygen oxidation in Co–Zn oxyhydroxide oxygen evolution electrocatalysts. *Nat Energy* **4**, 329–338 (2019).

21. B. Zhang, L. Wang, Z. Cao, S. M. Kozlov, F. P. García de Arquer, C. T. Dinh, J. Li, Z. Wang, X. Zheng, L. Zhang, Y. Wen, O. Voznyy, R. Comin, P. De Luna, T. Regier, W. Bi, E. E. Alp, C.-W. Pao, L. Zheng, Y. Hu, Y. Ji, Y. Li, Y. Zhang, L. Cavallo, H. Peng, E. H. Sargent, High-valence metals improve oxygen evolution reaction performance by modulating 3d metal oxidation cycle energetics. *Nat Catal* **3**, 985–992 (2020).

22. B. Zhang, X. Zheng, O. Voznyy, R. Comin, M. Bajdich, M. García-Melchor, L. Han, J. Xu, M. Liu, L. Zheng, F. P. García de Arquer, C. T. Dinh, F. Fan, M. Yuan, E. Yassitepe, N. Chen, T. Regier, P. Liu, Y. Li, P. De Luna, A. Janmohamed, H. L. Xin, H. Yang, A. Vojvodic, E. H. Sargent, Homogeneously dispersed multimetal oxygen-evolving catalysts. *Science* **352**, 333–337 (2016).

23. S. Pan, H. Li, D. Liu, R. Huang, X. Pan, D. Ren, J. Li, M. Shakouri, Q. Zhang, M. Wang, C. Wei, L. Mai, B. Zhang, Y. Zhao, Z. Wang, M. Graetzel, X. Zhang, Efficient and stable noble-metal-free catalyst for acidic water oxidation. *Nat Commun* **13**, 2294 (2022).

24. J. Huang, H. Sheng, R. D. Ross, J. Han, X. Wang, B. Song, S. Jin, Modifying redox properties and local bonding of $Co_3O_4$ by $CeO_2$ enhances oxygen evolution catalysis in acid. *Nat Commun* **12**, 3036 (2021).

25. L. Chong, G. Gao, J. Wen, H. Li, H. Xu, Z. Green, J. D. Sugar, A. J. Kropf, W. Xu, X.-M. Lin, H. Xu, L.-W. Wang, D.-J. Liu, La- and Mn-doped cobalt spinel oxygen evolution catalyst for proton exchange membrane electrolysis. *Science* **380**, 609–616 (2023).

26. A. Li, H. Ooka, N. Bonnet, T. Hayashi, Y. Sun, Q. Jiang, C. Li, H. Han, R. Nakamura, Stable Potential Windows for Long-Term Electrocatalysis by Manganese Oxides Under Acidic Conditions. *Angewandte Chemie International Edition* **58**, 5054–5058 (2019).

27. I. A. Moreno-Hernandez, C. A. MacFarland, C. G. Read, K. M. Papadantonakis, B. S. Brunschwig, N. S. Lewis, Crystalline nickel manganese antimonate as a stable water-oxidation catalyst in aqueous 1.0 M $H_2SO_4$. *Energy Environ Sci* **10**, 2103–2108 (2017).

28. I. C. Man, H.-Y. Su, F. Calle-Vallejo, H. A. Hansen, J. I. Martínez, N. G. Inoglu, J. Kitchin, T. F. Jaramillo, J. K. Nørskov, J. Rossmeisl, Universality in Oxygen Evolution Electrocatalysis on Oxide Surfaces. *ChemCatChem* **3**, 1159–1165 (2011).

29. J. S. Mondschein, J. F. Callejas, C. G. Read, J. Y. C. Chen, C. F. Holder, C. K. Badding, R. E. Schaak, Crystalline Cobalt Oxide Films for Sustained Electrocatalytic Oxygen Evolution under Strongly Acidic Conditions. *Chemistry of Materials* **29**, 950–957 (2017).

30. M. Etzi Coller Pascuzzi, M. van Velzen, J. P. Hofmann, E. J. M. Hensen, On the Stability of $Co_3O_4$ Oxygen Evolution Electrocatalysts in Acid. *ChemCatChem* **13**, 459–467 (2021).

31. N. Wang, P. Ou, R. K. Miao, Y. Chang, Z. Wang, S.-F. Hung, J. Abed, A. Ozden, H.-Y. Chen, H.-L. Wu, J. E. Huang, D. Zhou, W. Ni, L. Fan, Y. Yan, T. Peng, D. Sinton, Y. Liu, H. Liang, E. H. Sargent, Doping Shortens the Metal/Metal Distance and Promotes OH Coverage in Non-Noble Acidic Oxygen Evolution Reaction Catalysts. *J Am Chem Soc* **145**, 7829–7836 (2023).

32. M. Chatti, J. L. Gardiner, M. Fournier, B. Johannessen, T. Williams, T. R. Gengenbach, N. Pai, C. Nguyen, D. R. MacFarlane, R. K. Hocking, A. N. Simonov, Intrinsically stable in situ generated electrocatalyst for long-term oxidation of acidic water at up to 80 °C. *Nat Catal* **2**, 457–465 (2019).

33. P.-Y. Cheng, Y.-C. Ting, C.-C. Cheng, D. Senthil Raja, S.-H. Lin, Y.-X. Yeh, J.-T. Su, S.-Y. Lu, Nitrogen-doped carbon armored Cobalt oxide hollow nanocubes electrochemically anchored on fluorine-doped tin oxide substrate for acidic oxygen evolution reaction. *J Colloid Interface Sci* **623**, 327–336 (2022).

34. B. Rodríguez-García, Á. Reyes-Carmona, I. Jiménez-Morales, M. Blasco-Ahicart, S. Cavaliere, M. Dupont, D. Jones, J. Rozière, J. R. Galán-Mascarós, F. Jaouen, Cobalt hexacyanoferrate supported on Sb-doped $SnO_2$ as a non-noble catalyst for oxygen evolution in acidic medium. *Sustain Energy Fuels* **2**, 589–597 (2018).

35. Y. Wen, C. Liu, R. Huang, H. Zhang, X. Li, F. P. García de Arquer, Z. Liu, Y. Li, B. Zhang, Introducing Brønsted acid sites to accelerate the bridging-oxygen-assisted deprotonation in acidic water oxidation. *Nat Commun* **13**, 4871 (2022).

36. J. Rossmeisl, Z.-W. Qu, H. Zhu, G.-J. Kroes, J. K. Nørskov, Electrolysis of water on oxide surfaces. *Journal of Electroanalytical Chemistry* **607**, 83–89 (2007).

37. Y. Ping, R. J. Nielsen, W. A. I. I. I. Goddard, The Reaction Mechanism with Free Energy Barriers at Constant Potentials for the Oxygen Evolution Reaction at the $IrO_2$ (110) Surface. *J Am Chem Soc* **139**, 149–155 (2017).

38. L. Shen, B. Lu, Y. Li, J. Liu, Z. Huang-fu, H. Peng, J. Ye, X. Qu, J. Zhang, G. Li, W. Cai, Y. Jiang, S. Sun, Interfacial Structure of Water as a New Descriptor of the Hydrogen Evolution Reaction. *Angewandte Chemie International Edition* **59**, 22397–22402 (2020).

39. Y.-H. Wang, S. Zheng, W.-M. Yang, R.-Y. Zhou, Q.-F. He, P. Radjenovic, J.-C. Dong, S. Li, J. Zheng, Z.-L. Yang, G. Attard, F. Pan, Z.-Q. Tian, J.-F. Li, In situ Raman spectroscopy reveals the structure and dissociation of interfacial water. *Nature* **600**, 81–85 (2021).

40. S. Kong, A. Li, J. Long, K. Adachi, D. Hashizume, Q. Jiang, K. Fushimi, H. Ooka, J. Xiao, R. Nakamura, Acid-stable manganese oxides for proton exchange membrane water electrolysis. *Nat Catal*, doi: 10.1038/s41929-023-01091-3 (2024).

41. L. Gao, C. Li, W. Huang, S. Mei, H. Lin, Q. Ou, Y. Zhang, J. Guo, F. Zhang, S. Xu, H. Zhang, MXene/Polymer Membranes: Synthesis, Properties, and Emerging Applications. *Chemistry of Materials* **32**, 1703–1747 (2020).

42. S. E. Kelch, R. E. Youngman, E. Ferrage, J. J. Basinski, J. Wang, L. Aristilde, Quantitative Spectroscopic Analysis of Water Populations in the Hydrated Nanopore Environments of a Natural Montmorillonite. *The Journal of Physical Chemistry C* **125**, 26552–26565 (2021).

43. K. Oka, T. Shibue, N. Sugimura, Y. Watabe, B. Winther-Jensen, H. Nishide, Long-lived water clusters in hydrophobic solvents investigated by standard NMR techniques. *Sci Rep* **9**, 223 (2019).

44. Q. Hu, H. Zhao, S. Ouyang, Understanding water structure from Raman spectra of isotopic substitution $H_2O/D_2O$ up to 573 K. *Physical Chemistry Chemical Physics* **19**, 21540–21547 (2017).

45. C.-Q. Li, S.-S. Yi, D. Chen, Y. Liu, Y.-J. Li, S.-Y. Lu, X.-Z. Yue, Z.-Y. Liu, Oxygen vacancy engineered $SrTiO_3$ nanofibers for enhanced photocatalytic $H_2$ production. *J Mater Chem A Mater* **7**, 17974–17980 (2019).

46. A. Moysiadou, S. Lee, C.-S. Hsu, H. M. Chen, X. Hu, Mechanism of Oxygen Evolution Catalyzed by Cobalt Oxyhydroxide: Cobalt Superoxide Species as a Key Intermediate and Dioxygen Release as a Rate-Determining Step. *J Am Chem Soc* **142**, 11901–11914 (2020).

47. C. Jing, T. Yuan, L. Li, J. Li, Z. Qian, J. Zhou, Y. Wang, S. Xi, N. Zhang, H.-J. Lin, C.-T. Chen, Z. Hu, D.-W. Li, L. Zhang, J.-Q. Wang, Electrocatalyst with Dynamic Formation of the Dual-Active Site from the Dual Pathway Observed by In Situ Raman Spectroscopy. *ACS Catal* **12**, 10276–10284 (2022).

48. M. Zhang, M. de Respinis, H. Frei, Time-resolved observations of water oxidation intermediates on a cobalt oxide nanoparticle catalyst. *Nat Chem* **6**, 362–367 (2014).

49. H. Liu, C. Li, D. Chen, P. Cui, F. Ye, J. Yang, Uniformly dispersed platinum-cobalt alloy nanoparticles with stable compositions on carbon substrates for methanol oxidation reaction. *Sci Rep* **7**, 11421 (2017).

50. S. Geiger, O. Kasian, M. Ledendecker, E. Pizzutilo, A. M. Mingers, W. T. Fu, O. Diaz-Morales, Z. Li, T. Oellers, L. Fruchter, A. Ludwig, K. J. J. Mayrhofer, M. T. M. Koper, S. Cherevko, The stability number as a metric for electrocatalyst stability benchmarking. *Nat Catal* **1**, 508–515 (2018).

51. C. Wei, Z. Wang, K. Otani, D. Hochfilzer, K. Zhang, R. Nielsen, I. Chorkendorff, J. Kibsgaard, Benchmarking Electrocatalyst Stability for Acidic Oxygen Evolution Reaction: The Crucial Role of Dissolved Ion Concentration. *ACS Catal* **13**, 14058–14069 (2023).

52. M. Milosevic, T. Böhm, A. Körner, M. Bierling, L. Winkelmann, K. Ehelebe, A. Hutzler, M. Suermann, S. Thiele, S. Cherevko, In Search of Lost Iridium: Quantification of Anode Catalyst Layer Dissolution in Proton Exchange Membrane Water Electrolyzers. *ACS Energy Lett* **8**, 2682–2688 (2023).

53. H. Benzidi, Co-del_OER. *ioChem-BD*, doi: 10.19061/iochem-bd-1-320 (2024).

54. R. Ram, F.P. García de Arquer, STEM and XRD files of Water and Hydroxide Trapping in Cobalt Tungstate for Proton Exchange Membrane Water Electrolysis. *Zenodo*, doi: 10.5281/zenodo.11161891 (2024).

55. G. Kresse, J. Hafner, Ab initio molecular dynamics for open-shell transition metals. *Phys Rev B* **48**, 13115–13118 (1993).

56. A. Togo, L. Chaput, T. Tadano, I. Tanaka, Implementation strategies in phonopy and phono3py. *Journal of Physics: Condensed Matter* **35**, 353001 (2023).

57. M. Garcia-Ratés, N. López, Multigrid-Based Methodology for Implicit Solvation Models in Periodic DFT. *J Chem Theory Comput* **12**, 1331–1341 (2016).

58. J. K. Nørskov, J. Rossmeisl, A. Logadottir, L. Lindqvist, J. R. Kitchin, T. Bligaard, H. Jónsson, Origin of the Overpotential for Oxygen Reduction at a Fuel-Cell Cathode. *J Phys Chem B* **108**, 17886–17892 (2004).

59. A. Li, S. Kong, C. Guo, H. Ooka, K. Adachi, D. Hashizume, Q. Jiang, H. Han, J. Xiao, R. Nakamura, Enhancing the stability of cobalt spinel oxide towards sustainable oxygen evolution in acid. *Nat Catal* **5**, 109–118 (2022).

60. Q. Yin, J. M. Tan, C. Besson, Y. V Geletii, D. G. Musaev, A. E. Kuznetsov, Z. Luo, K. I. Hardcastle, C. L. Hill, A Fast Soluble Carbon-Free Molecular Water Oxidation Catalyst Based on Abundant Metals. *Science* **328**, 342–345 (2010).

61. Z. Kang, T. Schuler, Y. Chen, M. Wang, F.-Y. Zhang, G. Bender, Effects of interfacial contact under different operating conditions in proton exchange membrane water electrolysis. *Electrochim Acta* **429**, 140942 (2022).

62. M. J. Burch, K. A. Lewinski, M. I. Buckett, S. Luopa, F. Sun, E. J. Olson, A. J. Steinbach, A novel work-flow to study Ir electrode thinning and dissolution in proton exchange membrane water electrolyzers. *J Power Sources* **500**, 229978 (2021).

63. J. Yu, F. A. Garcés-Pineda, J. González-Cobos, M. Peña-Díaz, C. Rogero, S. Giménez, M. C. Spadaro, J. Arbiol, S. Barja, J. R. Galán-Mascarós, Sustainable oxygen evolution electrocatalysis in aqueous 1 M $H_2SO_4$ with earth abundant nanostructured $Co_3O_4$. *Nat Commun* **13**, 4341 (2022).

64. K.-L. Yan, J.-F. Qin, J.-H. Lin, B. Dong, J.-Q. Chi, Z.-Z. Liu, F.-N. Dai, Y.-M. Chai, C.-G. Liu, Probing the active sites of Co3O4 for the acidic oxygen evolution reaction by modulating the $Co^{2+}/Co^{3+}$ ratio. *J Mater Chem A Mater* **6**, 5678–5686 (2018).

65. M. Blasco-Ahicart, J. Soriano-López, J. J. Carbó, J. M. Poblet, J. R. Galan-Mascaros, Polyoxometalate electrocatalysts based on earth-abundant metals for efficient water oxidation in acidic media. *Nat Chem* **10**, 24–30 (2018).

66. Y. Yang, H. Yao, Z. Yu, S. M. Islam, H. He, M. Yuan, Y. Yue, K. Xu, W. Hao, G. Sun, H. Li, S. Ma, P. Zapol, M. G. Kanatzidis, Hierarchical Nanoassembly of $MoS_2/Co_9S_8/Ni_3S_2$/Ni as a Highly Efficient Electrocatalyst for Overall Water Splitting in a Wide pH Range. *J Am Chem Soc* **141**, 10417–10430 (2019).

67. F. Hu, S. Zhu, S. Chen, Y. Li, L. Ma, T. Wu, Y. Zhang, C. Wang, C. Liu, X. Yang, L. Song, X. Yang, Y. Xiong, Amorphous Metallic NiFeP: A Conductive Bulk Material Achieving High Activity for Oxygen Evolution Reaction in Both Alkaline and Acidic Media. *Advanced Materials* **29**, 1606570 (2017).

## SUPPLEMENTARY MATERIALS

**Figures S1 to S81**

**Movie S1**

**Tables S1 to S22**

**References (55-67)**

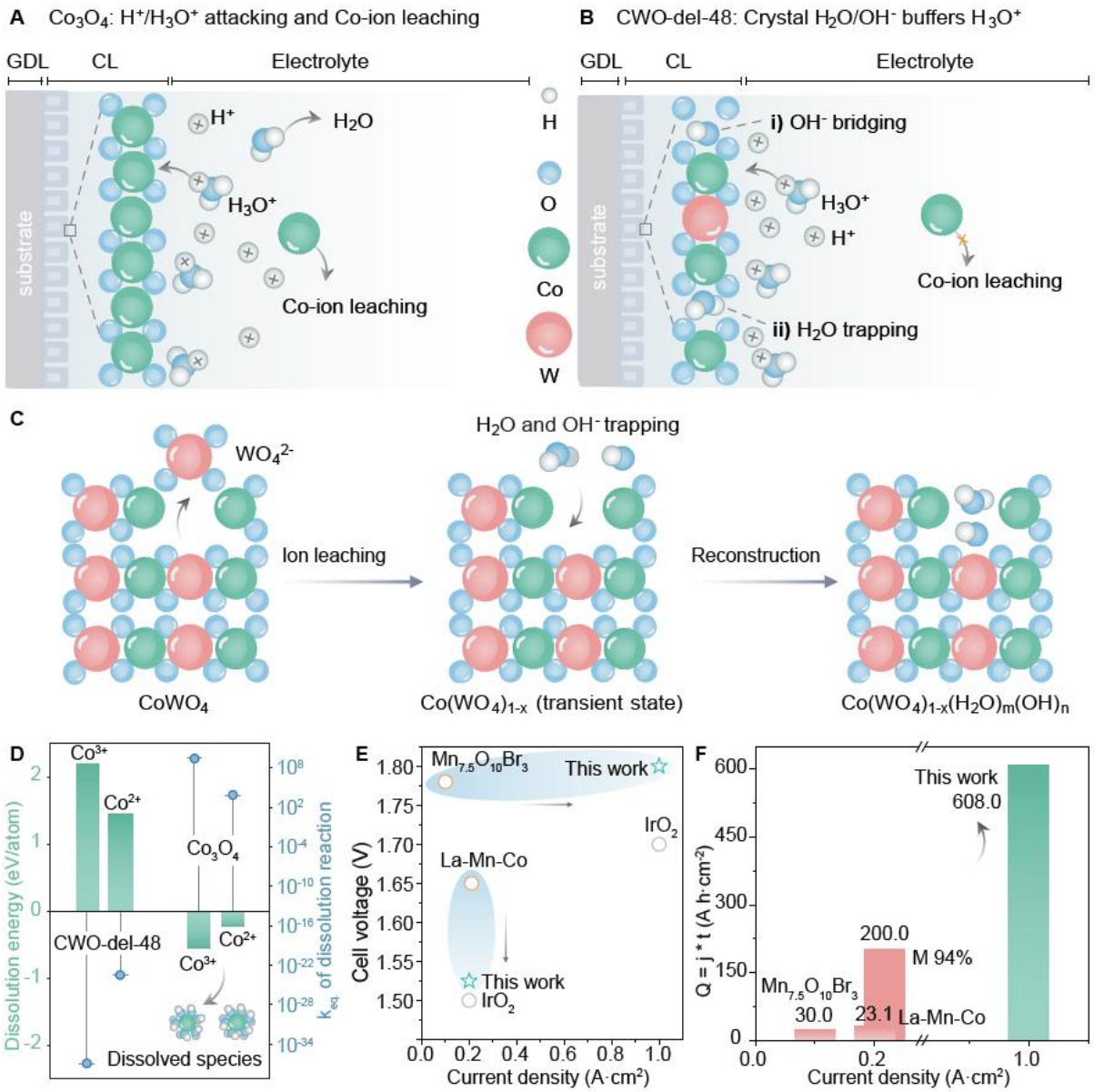


**Fig. 1. Water-hydroxide trapping enables active and stable Proton Exchange Membrane Water Electrolysis. (A)** Schematic illustration of the dissolution of Co ions in $Co_3O_4$ via Co–O bond cleaving, followed by their hydration in acidic medium. **(B)** A depiction of delaminated cobalt catalysts (CWO–del–48) illustrating the effect of water trapping and hydroxide bridging within the crystal lattice, enabling stability in acid. **(C)** The process and the crystallographic representation of CWO delamination into CWO–del–48 via base treatment. **(D)** CWO–del–48 catalyst shows unfavorable Co ions dissolution compared to $Co_3O_4$. The calculated equilibrium constants of dissolution reaction for CWO–del–48, $K_{eq} << 1$, suggesting non-spontaneity of the process. The structure of dissolved $Co^{2+}$ and $Co^{3+}$ ions are shown in the inset. This equilibrium enables significant advances in performance **(E)** cell voltage *vs.* current density, and **(F)** durability, compared to state-of-the-art Ir and Ru-free anodes in PEMWE.

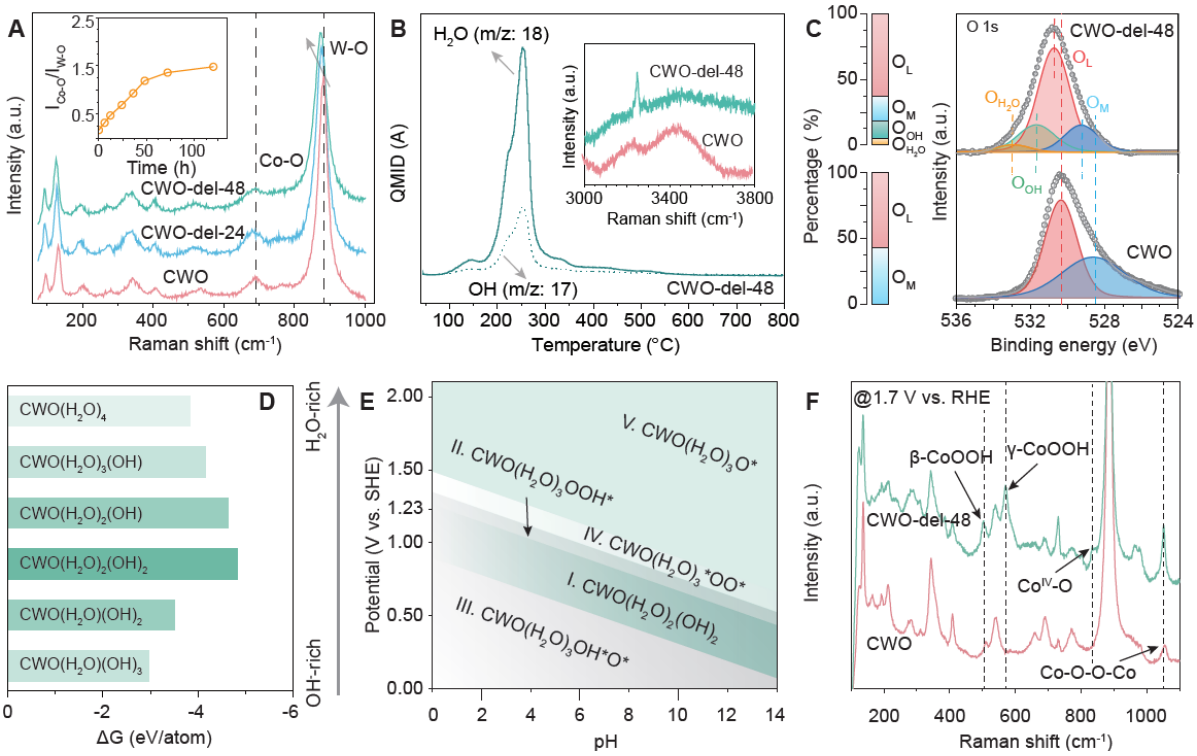


**Fig. 2. Water trapping and hydroxide bridging. (A)** *Ex situ* Raman spectra of as-synthesized CWO and CWO–del (24 h and 48 h) showing a regular red shift associated with the W-O vibrational peaks. Inset: intensity ratio of the Co–O and W–O peaks with delamination time. **(B)** Thermogravimetric analysis coupled with mass spectrometry (TGA-MS) shows the presence of $H_2O$ and hydroxide in CWO–del–48. Inset: *ex situ* Raman spectra showing presence of different types of water. The sharp H–OH stretching peak of CWO–del–48 indicates presence of strongly H-bonded water. **(C)** O 1s XPS spectra of CWO and CWO–del–48. O 1s peak in CWO deconvolutes into metal-oxygen ($O_M$) and lattice-oxygen ($O_L$). O 1s peak in CWO–del–48 deconvolutes into four peaks: $O_M$, $O_L$, hydroxide ($O_{OH}$) and water ($O_{H2O}$). **(D)** Visual representation of the free energy changes involved in the delamination process of CWO to $CWO(H_2O)_m(OH)_n$ under alkaline solution, as a result of water trapping and hydroxide bridging with the removal of tungstate (see suppl. Movie 1). DFT simulations predict that $CWO(H_2O)_2(OH)_2$ is the thermodynamically the most favorable composition for CWO–del–48. (**E**) Potential and pH dependence of the intermediates in OER for the CWO–del–48. **(G)** *In situ* Raman spectra of CWO and CWO–del–48 catalysts at 1.7 V *vs.* RHE suggests the involvement of Co (III), Co (IV), and Co-peroxide, as the active-OER species.

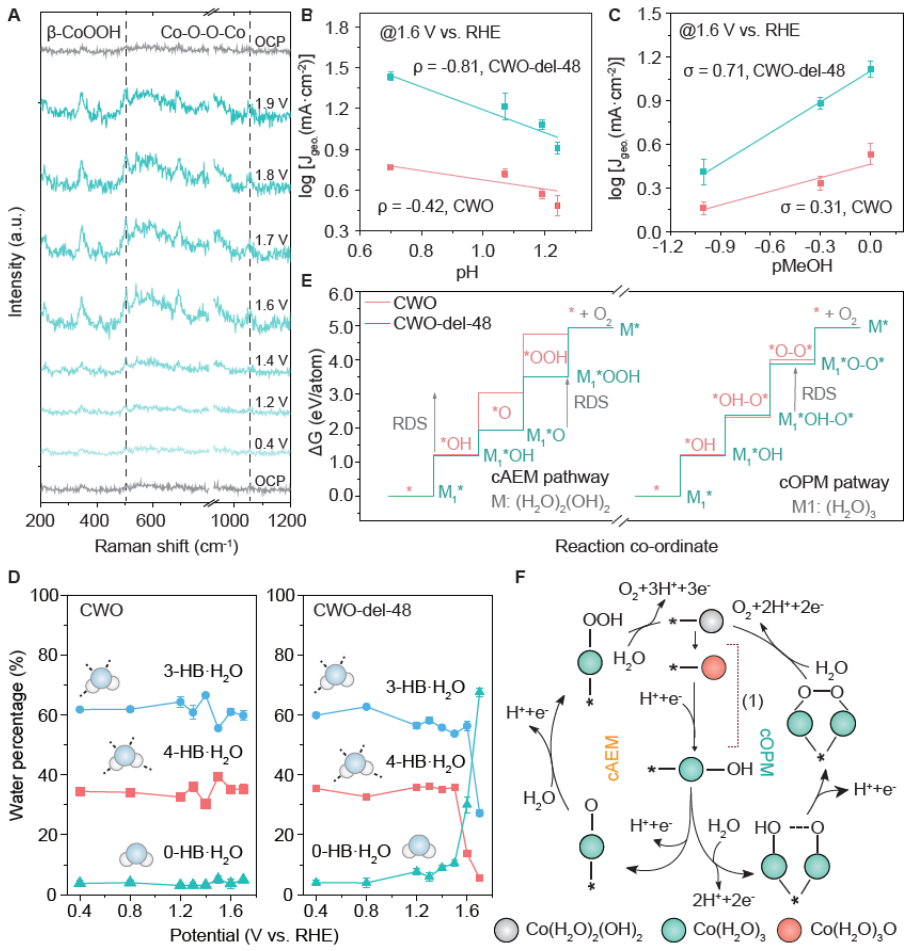


**Fig. 3. OER reaction mechanism: operando and DFT studies. (A)** *Operando* Raman spectroscopy in CWO–del–48 (on carbon paper, from OCP to 1.9 V *vs.* RHE in 0.5 M $H_2SO_4$), reveals a correlation between OER activity and the intensity of β–CoOOH and Co–O–O–Co peaks. pH-dependent studies (1.6 V *vs.* RHE as a function of pH) during **(B)** OER and **(C)** Methanol Oxidation Reaction (MOR) elucidate the role of surface-trapped water fragments. Error bars correspond to the standard deviation and average of three independent measurements. **(D)** Percentage of different type of interfacial water structure with applied potential for CWO (left) and CWO–del–48 (right). In CWO-del, the % of 0-HB·$H_2O$ water increases with applied potential while 4-HB·$H_2O$ structure decreases. These remain almost unchanged for CWO in the applied potential window. **(E)** Free energy profiles of CWO and CWO–del–48 in OER reaction pathways. The involved species and/or intermediates are shown in the corresponding steps. The dynamic involvement of $H_2O$ and $OH^-$ enables favorable cAEM and cOPM reaction pathways in CWO–del–48. **(F)** OER catalytic cycle schematically showing the cAEM and cOPM pathways. The first step is the chemical conversion of *$Co(H_2O)_2(OH)_2$ to *$Co(H_2O)_3O$. Both the cAEM and cOPM mechanisms share *$Co(H_2O)_3$–OH as a common intermediate.

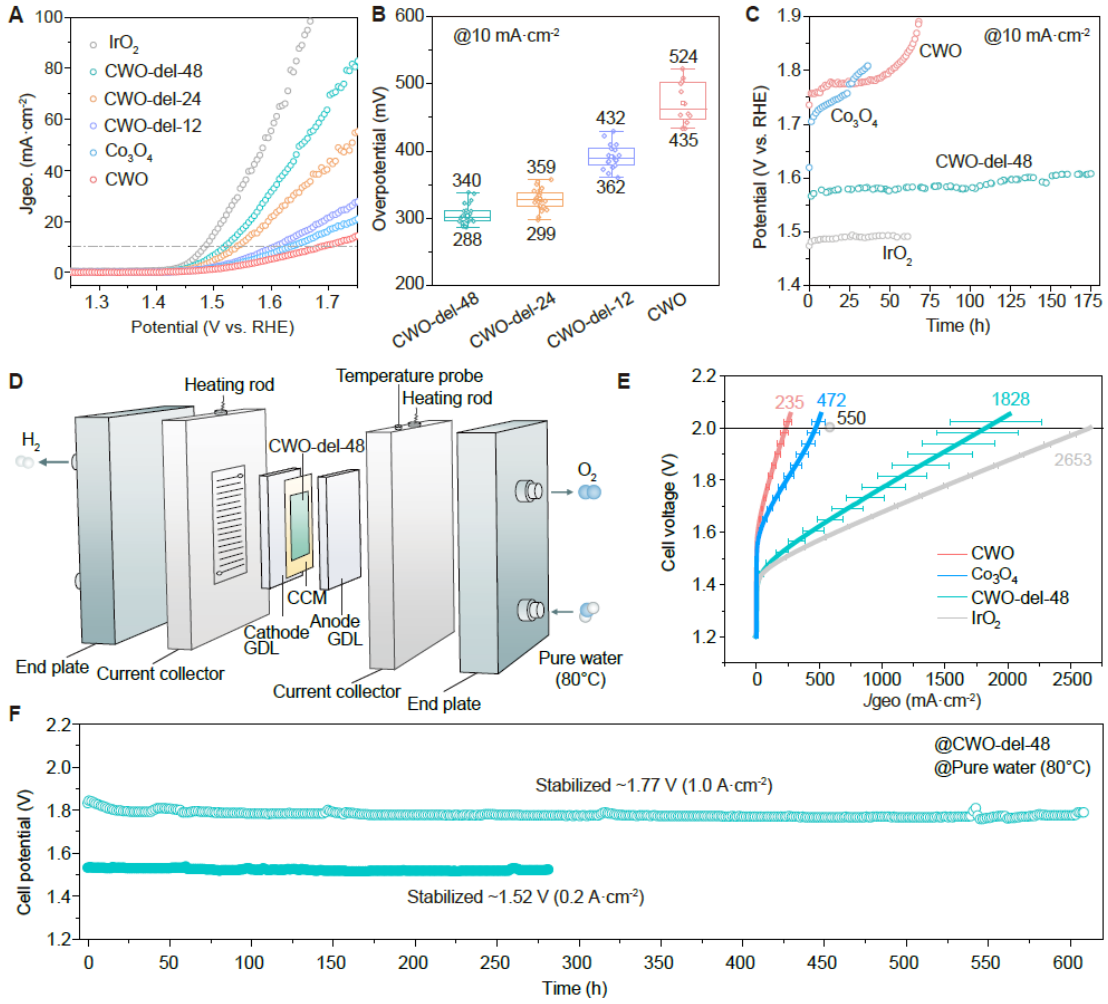


**Fig. 4. Electrochemical performance and stable PEMWE at the ampere-level. (A)** Linear-sweep voltammetry of Co-based catalysts at 5 $mV \cdot s^{-1}$ in 0.5 M $H_2SO_4$ electrolyte along with commercial $IrO_2$ and $Co_3O_4$ (no *iR*-correction) **(B)** Overpotential statistics at 10 $mA \cdot cm^{-2}$ current density. **(C)** Chronopotentiometry stability tests in 0.5 M $H_2SO_4$ electrolyte at constant 10 $mA \cdot cm^{-2}$ current density in H-cell set up using a Nafion 117 membrane. **(D)** Illustration of PEMWE along with catalyst coated membrane (CCM), cathode and anode GDL. **(E)** The PEMWE based polarization curves of CWO–del–48, CWO, commercial $Co_3O_4$ and $IrO_2$ (without *iR*-correction), used as anodic material separately. The PEMWE based polarization curve is compared with the best reported, La, Mn co-doped porous cobalt spinel fibers catalyst (*25*). Commercial 60 wt.% Pt/C was used as cathodic material and Nafion 117 is the membrane. **(F)** The chronopotentiometry stability test of CWO–del–48 at 0.2 $A \cdot cm^{-2}$ and at 1.0 $A \cdot cm^{-2}$ of current density in PEMWE at 80˚C temperature for 278 h and 608 h, respectively, after overnight conditioning at 1.7 V (see suppl. methods for details). The milli-Q water filling process during operation leads to small voltage transients due to temperature gradients and interface re-equilibration.